J Nanopart Res (2014) 16:2322
DOI 10.1007/s11051-014-2322-5

RESEARCH PAPER

Enhanced magnetic coercivity of α-Fe_2O_3 obtained from carbonated 2-line ferrihydrite

B. Vallina · J. D. Rodriguez-Blanco · A. P. Brown · L. G. Benning · J. A. Blanco

Received: 6 May 2013 / Accepted: 5 February 2014

Abstract We report the physical properties of α-Fe_2O_3 (hematite), synthesized by dry-heating (350–1,000 °C) of a new, poorly ordered iron oxyhydroxide precursor compound that we name carbonated 2-line ferrihydrite. This precursor was characterized by powder X-ray diffraction, Fourier transform infrared spectroscopy, electron microscopy, and thermogravimetric analysis, whereas the α-Fe_2O_3 was studied with X-ray diffraction, scanning and transmission electron microscopy, and magnetic techniques. α-Fe_2O_3 synthesized at 350 °C consisted of single-nanocrystal particles (length × width 20 ± 6 nm (L) × 15 ± 4 nm (W)), which at room temperature exhibited very narrow hysteresis loops of low coercivities (<300 Oe). However, α-Fe_2O_3 synthesized at higher temperatures (1,000 °C) was composed of larger nanocrystalline particle aggregates (352 ± 109 nm (L) × 277 ± 103 nm (W)) that also showed wide-open hysteresis loops of high magnetic coercivities (~5 kOe). We suggest that these synthesis-temperature-dependent coercivity values are a consequence of the subparticle structure induced by the different particle and crystallite size growth rates at increasing annealing temperature.

Keywords Hematite · Ferrihydrite · High coercivity · Carbonate · Microstructure

Electronic supplementary material The online version of this article (doi:10.1007/s11051-014-2322-5) contains supplementary material, which is available to authorized users.

B. Vallina · J. D. Rodriguez-Blanco · L. G. Benning
School of Earth and Environment, University of Leeds, Leeds LS2 9JT, UK

B. Vallina (✉) · J. A. Blanco
Departamento de Física, Universidad de Oviedo, 33007 Oviedo, Spain
e-mail: eebva@leeds.ac.uk

J. A. Blanco
e-mail: jabr@uniovi.es

J. D. Rodriguez-Blanco
Department of Chemistry, Nano-Science Center, University of Copenhagen H.C Oersted Institute, C Bygn, Universitetsparken 5, 2100 Kopenhagen, Denmark

A. P. Brown
Faculty of Engineering, Institute for Materials Research, SPEME, University of Leeds, Leeds LS2 9JT, UK

Introduction

Iron oxides are very widespread in nature and they have attracted considerable attention in various scientific disciplines particularly due to the unique combination of electronic, chemical, optical, and thermal properties (Cornell and Schwertmann 2003). Among the sixteen known iron oxy(hydro)xides (Cornell and Schwertmann 2003), α-Fe_2O_3 (hematite) is considered the ideal candidate for many technological applications due to its low cost, biodegradability, high resistance to corrosion, and high stability (e.g., Gubin et al. 2005; Zhu et al. 2011; Jacob and Khadar 2010).

Published online: 20 February 2014

Over the last decade, research efforts were focused on the development of α-Fe_2O_3-bearing materials with potential technological applications in catalysis (Fang et al. 2009), hydrocarbon and carbon monoxide gas sensors (e.g., Cornell and Schwertmann 2003), pigments (e.g., Ni et al. 2009), water treatment (e.g., Guo et al. 2011), rechargeable batteries (Pan et al. 2009), adsorbents (Muruganandham et al. 2011), biomedicine (e.g., Liu et al. 2011), semiconductors (e.g., Bahgat et al. 2006), or optical and electromagnetic devices (e.g., Tsuzuki et al. 2011). Despite this plethora of research, some of the magnetic properties of synthetic α-Fe_2O_3 are still not fully understood (Lovesey et al. 2011; Tadic et al. 2012).

α-Fe_2O_3 is weakly ferromagnetic at ambient temperature with a Neel temperature of $\sim$953 K (Xu et al. 2009). However, α-Fe_2O_3 changes from weakly ferromagnetic to antiferromagnetic below room temperature, a magnetic phase transition known as the Morin transition (Cornell and Schwertmann 2003). This Morin transition temperature decreases with particle size, and it is completely suppressed when the α-Fe_2O_3 particles become smaller than $\sim$20 nm (Tadic et al. 2011, 2012; Bercoff and Bertorello 2010). Similarly to the Morin transition temperature, other magnetic properties of α-Fe_2O_3 can dramatically change with particle or Scherrer crystallite size, particle morphology, interparticle interactions, synthesis pressure, or with doping (Jacob and Khadar 2010; Sahu et al. 1997; Suber et al. 2010; Chang et al. 2010). For example, depending on the preparation method (e.g., hydrothermal synthesis *vs.* mechanical grinding), particle morphology, or particle microstructure can lead to magnetic coercivities for α-Fe_2O_3 as high as a few kOe (e.g., Rath et al. 1999; Yang et al. 2011). Most studies suggest that the presence of a subparticle structure in the α-Fe_2O_3 nanocrystals may explain such high coercivities. However, this is still a matter of debate, as the correlation between morphology, microstructure, particle interactions, and magnetic properties of α-Fe_2O_3 are still ambiguous and the exact reasons for this behavior are not fully understood.

The next needed development is the design and testing of novel methods for controlled synthesis of α-Fe_2O_3 nanocrystals with specific chemical, physical, and magnetic properties that can be exploited for potential technological applications. Most studies that addressed the synthesis of α-Fe_2O_3 employed a solvothermal approach (An et al. 2012; Mitra et al. 2007; Xu and Zhu 2012; Wang et al. 2011; Zhang and Chen 2009) or hydrothermal methods (e.g., Tadi et al. 2011; Song et al. 2009, 2011; Li et al. 2007, 2009; Ni et al. 2012; Peng et al. 2010; Davidson et al. 2008; Vu et al. 2010; Zhu et al. 2006; Zhong et al. 2008; Zhang et al. 2008; Jia and Song 2012, 2011; Lu et al. 2008; Islam et al. 2012; Suresh et al. 2013 and references therein). In recent years, producing α-Fe_2O_3 via dry thermal treatments of iron-bearing precursor phases has become a common synthesis method. An iron oxyhydroxide precursor phase that is very common in both natural environments and laboratory synthesis studies is the poorly ordered phase ferrihydrite. Its precise chemical formula and structure are the subject of much recent debate (Cornell and Schwertmann 2003; Yu et al. 2002; Berquó et al. 2007; Liu et al. 2009; Michel et al. 2010) in part because ferrihydrite is the crucial precursor for α-Fe_2O_3—the mineral hematite. This poorly crystalline phase is usually termed as 2- or 6-line ferrihydrite according to the number of broad Bragg peaks observed in its powder X-ray diffraction pattern (Cornell and Schwertmann 2003). To synthesize ferrihydrite in the laboratory, three different methods are usually employed: (a) neutralizing a ferric salt solution (e.g., Stanjek and Weidler 1992; Zhao et al. 1994; Carta et al. 2009; Xu et al. 2011), (b) dialyzing a ferric nitrate solution (e.g., Cornell and Schwertmann 2003), or (c) oxidizing a ferrous salt solution (Schwertmann and Taylor 1972). Once 2- or 6-line ferrihydrite is synthesized, it is crystallized to α-Fe_2O_3 by dry heating (Stanjek and Weidler 1992; Schneeweiss et al. 2008) either through hydrothermal routes (e.g., Vu et al. 2010; Xu et al. 2011) or through slow aging in solution (Raiswell et al. 2010). However, most of these studies had the primary goal to only characterize the ferrihydrite structure or stability and not the properties of the final product, α-Fe_2O_3.

In this current study, we took a two-step approach. We designed and tested a novel method that allowed us to produce α-Fe_2O_3 with high magnetic coercivities from a precursor 2-line ferrihydrite, yet this precursor was itself produced via a novel green-chemical method in the presence of carbonate. This carbonated 2-line ferrihydrite precursor was formed following an equivalent methodology to an often employed approach used for the production of amorphous carbonate or phosphate precursors (Rodriguez-Blanco et al. 2008; Vallina et al. 2013; Roncal-Herrero et al.

2009). After synthesis, the resulting solids were dry-heated from 350 to 1,000 °C, and the crystalline product, α-Fe_2O_3, was characterized with X-ray diffraction, high-resolution microscopy, and magnetometry. A correlation between the magnetic properties of this novel α-Fe_2O_3 and its structure at the nanoscale is reported and discussed.

Experimental

The synthesis of α-Fe_2O_3 was performed in two steps: first, an aqueous solution containing 50 mM of $Fe(NO_3)_3{\cdot}9H_2O$ (Sigma-Aldrich, 99.9 % purity) was added to an aqueous solution containing 50 mM of Na_2CO_3 (Fisher Scientific, 99.9 % purity) at ambient temperature. The mixed solutions were rapidly filtered under vacuum through 0.2 μm polycarbonate membranes, obtaining a dark reddish precipitate. This solid was immediately washed with Milli-Q water and isopropanol and dried at room temperature, following Rodriguez-Blanco et al. (2008). The so-obtained dry solids were dry-heated to specific temperatures (350, 600, 800, and 1,000 °C) following a 3 h thermal equilibration and then allowed to cool down to room temperature.

The initial precipitate and the temperature-dependent crystalline end products were identified by powder X-ray diffraction (XRD) using a Panalytical X′Pert Pro diffractometer ($CuK\alpha_{1,2}$; 2θ range 20–70; 0.01°/step and 0.3 s/step). In order to also follow the crystallization of the initial precursor phase to α-Fe_2O_3 and to identify any potential intermediate phase transformations during the heating process, we also employed the same diffractometer with an additional Anton Paar HTK 1200 N High-Temperature Oven-Chamber and carried out powder X-ray thermodiffraction. Thermodiffraction patterns were collected from 25 to 1,000 °C (at a constant heating ramp of 1 °C/min; 2θ range 20–50 at 0.01°/step and 0.16 s/step) while running the system at atmospheric conditions. Pattern-matching refinement of the crystalline phases was carried out using the Rietveld refinement software TOPAS (Coelho 2003). Crystallite sizes were estimated from the diffraction patterns using the Scherrer equation (Scherrer 1918), with the assumption that the particles were stress-free and taking into account the X-ray pattern of a LaB_6 standard (ICDD PDF 34-0427; $2\theta_{110} = 30.36°$ and FWHM = 0.06°). The precursor phase was also analyzed with Fourier transform infrared (FTIR) spectroscopy, thermogravimetric analyses (TGA), and transmission electron microscopy (TEM). FTIR spectra were acquired on an A2-Technology Microlab Portable mid-IR spectrometer with a Diamond internal reflection cell (DATR). FTIR spectra were collected by co-adding 1,024 scans in the 650–4,000 cm^{-1} range at a resolution of 4 cm^{-1}. The Thermo Nicolet OMNIC ESP 5.1 software package was used to manipulate the spectra, including baseline subtraction. Thermogravimetric analyses were carried out with a Mettler TA 4,000 instrument, while heating the samples from 25 to 1,000 °C at a rate of 10 °C/min in nitrogen atmosphere. Finally, using a field emission gun transmission electron microscope (FEG-TEM; FEI CM200; operated at 197 kV and equipped with Oxford Instruments energy-dispersive X-ray (EDX) analysis system (Isis) and a Gatan Imaging Filter (GIF-200)), the precursor phase was imaged and spectrally analyzed.

Complementing the data set of the precursor phase, we also imaged and analyzed the morphology and structural characteristics of the crystalline end product phases using an FEG scanning electron microscope (FEG-SEM, LEO 1530 Gemini, operated at 3 kV and with an in-lens detector, equipped with an energy-dispersive X-ray (EDX) analysis system; Isis) and a high-resolution TEM (HR-TEM; MET JEOL-JEM 2100F, with an in-lens detector, equipped with an energy-dispersive X-ray (EDX) analysis system). Finally, the temperature-dependent crystalline end products were fully characterized for their magnetic properties at room temperature using a vibrating sample magnetometer (EV9 VSM) with a maximum magnetic field of 20 kOe. Magnetic hysteresis measurements were conducted in an applied magnetic field sweeping from −20 to 20 kOe.

Results and discussion

Characterization of carbonate bearing-ferrihydrite

High-resolution TEM images of the dark reddish precipitate that formed immediately upon mixing of the starting solutions revealed that it consisted of agglomerates of nanoparticles (<20 nm in size) of amorphous to nanocrystalline character (Fig. 1). Standarless quantification of EDX spectra indicated

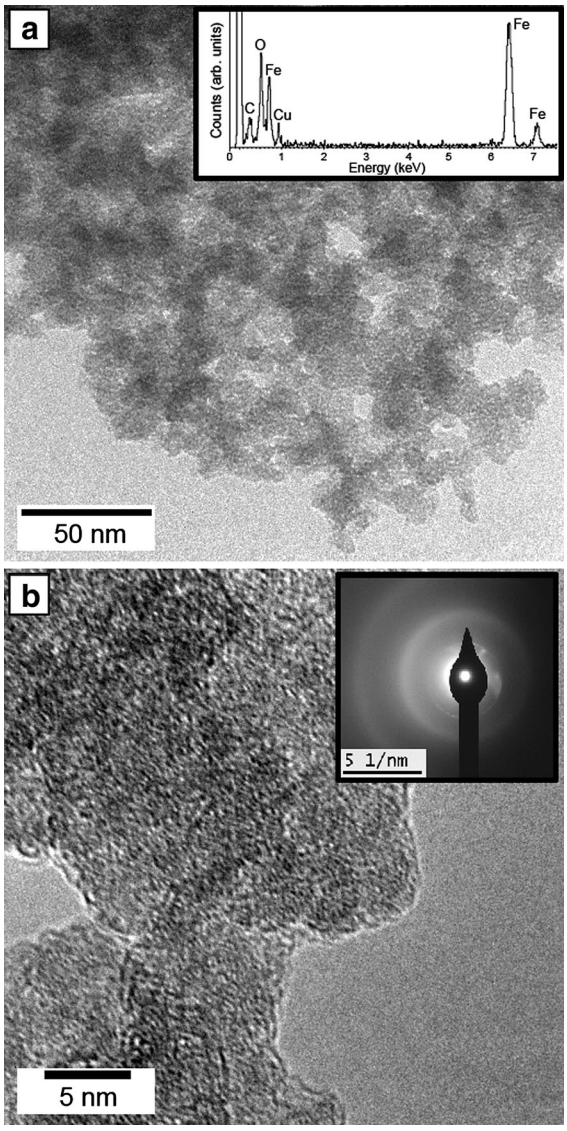

Fig. 1 TEM images of carbonated 2-line ferrihydrite. The *top* and *bottom insets* show the EDX spectrum (Cu signal comes from the Cu support grid) and SAED pattern obtained from the sample

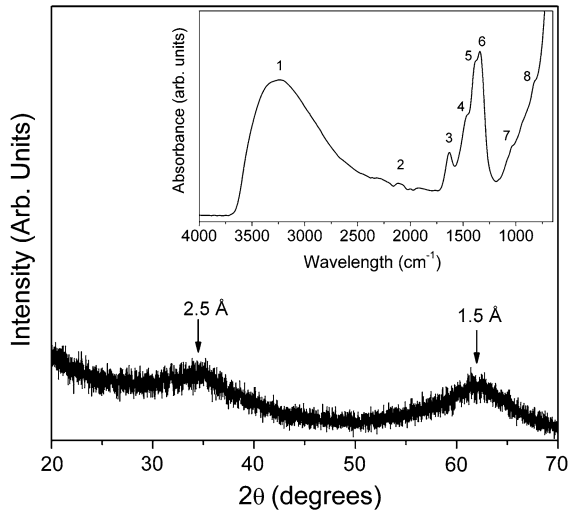

Fig. 2 Powder X-ray diffraction pattern of the carbonated 2-line ferrihydrite. Inset: FTIR spectrum of carbonated 2-line ferrihydrite precursor. The band assignments are detailed in Table 1

a ~24 % C, ~34 % O, and ~38 % Fe content (Fig. 1a, inset) and Electron Energy Loss Spectroscopy (EELS) suggested some carbonate (from the sharp peak at ~290 eV at the C K-edge) plus a ferrihydrite structure (O K-edge) that was predominately ferric (Fe L-edge), with amorphous or disordered carbon adsorbed or co-precipitated (Fig. SI-1). Selected area electron diffraction (SAED) patterns showed two broad diffuse rings at ~1.5 and 2.5 Å consistent with a 2-line ferrihydrite pattern (Cornell and Schwertmann 2003). High magnification images also revealed small particles with diffuse lattice fringes (Fig. 1b).

Powder X-ray diffraction of this initial amorphous material (Fig. 2) showed two broad humps centered at approximately 35° and 63° 2θ, consistent with the amorphous to nanocrystalline nature of the carbon containing 2-line ferrihydrite identified by TEM. The FTIR spectrum of this 2-line ferrihydrite (Table 1; Fig. 2, inset) was characterized by the broad and prominent band in the range ~3,700 and 2,300 cm^{-1} and the band at ~1,633 cm^{-1}, which were ascribed to the stretching and bending of OH groups, respectively. These bands were attributed to adsorbed or structural water (Liu et al. 2009; Farmer 1974). The bands at ~1,385 and 1,338 cm^{-1} were assigned to Fe–OH vibrations. The spectrum also showed a weak band at 824 cm^{-1}, which was attributed to the bending vibration of hydroxyl groups of iron hydroxides (Fe–OH) (Rout et al. 2012). Interestingly, the FTIR spectra revealed the presence of carbonate bonds in association with the 2-line ferrihydrite precursor. This is evidenced in the weak bands at ~1,455 and 1,042 cm^{-1}, which are typical of the stretching vibrations of the carbonate ion (Farmer 1974). Such carbonate bands are often observed in ferrihydrite FTIR spectra because of its susceptibility to CO_2 adsorption from air (Liu et al. 2009). However, in our

Table 1 FTIR stretching (ν) and bending (δ) vibrational bands for carbonated 2-line ferrihydrite

Band number	Wavelength (cm^{-1})	Mode of vibration	Bibliography
1	3,700–2,300	ν (O–H)	Liu et al. (2009); Farmer (1974)
2	2,463–2,332	ν CO_2	Yadav (2005)
3	1,633	δ (O–H)	Farmer (1974)
4	1,455	ν_3 asym. CO_3	Liu et al. (2009); Andersen and Brečević (1991)
5	1,385	Fe–OH	Rout et al. (2012)
6	1,338	Fe–OH	Rout et al. (2012)
7	1,042	ν_1 CO_3	Andersen and Brečević (1991)
8	824	δ (Fe–OH)	Rout et al. (2012)

case, the high percentage of C detected by TEM—EELS (Fig. SI-1) suggests that the carbonate adsorbed or co-precipitated with our 2-line ferrihydrite. Thus, our FTIR spectra did not just reveal atmospheric CO_2 adsorption, but indicates carbonate that is closely associated with the 2-line ferrihydrite and thus we suppose the carbonate seen in the spectra must have been derived from the Na_2CO_3 reagent used in our synthesis.

The TGA data of the 2-line ferrihydrite (Fig. 3) showed that upon heating a total weight loss of approximately ~35 % occurred of which ~10 % was lost below 100 °C and the other ~25 % was lost between 100 and 480 °C, after which no more changes were observed. Although little is known about the dehydration of 2-line ferrihydrite, the weight loss of our solid during the TGA analyses was slightly higher than values (23–25 %) reported by other authors (Carta et al. 2009; Xu et al. 2011; Eggleton and Fitzpatrick 1988). The high water content in our 2-line ferrihydrite that was confirmed by our FTIR data (Fig. 2, inset) indicates a weight loss with increasing temperature consistent with dehydration (Cornell and Schwertmann 2003; Carta et al. 2009; Eggleton and Fitzpatrick 1988). However, both HR-TEM and FTIR data clearly indicated a carbonate association with the 2-line ferrihydrite (Figs. 1, 2 inset and Fig. S1). Thus, we hypothesize that part of the weight loss must be a consequence of the decomposition of CO_3 to CO_2. This carbonate loss is predicted to occur above 300 °C

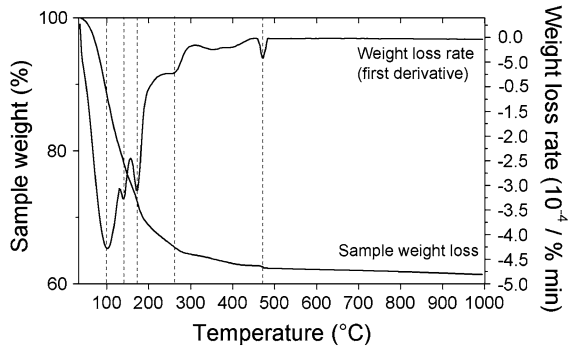

Fig. 3 TGA (sample weight loss and weight loss rate curves) of carbonated 2-line ferrihydrite

(Galwey and Brown 1999) and can be seen to happen in our samples at ~480 °C (Fig. 3 the first derivative curve).

Taken as a whole, the XRD, HR-TEM, FTIR, and TGA data point toward a new compound that we label, carbonated 2-line ferrihydrite, consistent with a previous report (Liu et al. 2008). It has to be noted that the structure and precise composition of our carbonated 2-line ferrihydrite are unknown. Indeed, the structures and formulas of all ferrihydrites are still the subject of intense debate (Cornell and Schwertmann 2003; Yu et al. 2002; Berquó et al. 2007; Liu et al. 2009; Michel et al. 2010) and so far no definitive consensus has been reached. Obtaining the exact formula or structural characteristics of our new, carbonate-rich 2-line ferrihydrite is outside the scope of this study.

Hematite properties synthesized from carbonated 2-line ferrihydrite

Our carbonated 2-line ferrihydrite was dry-heated from 25 to 1,000 °C, with simultaneous recording of thermo-diffraction patterns (Fig. 4). Initially, the XRD patterns exhibited only a large background hump (at ~35° 2θ) with no distinct diffraction peaks and no detectable change upon heating up to 250 °C. Only at higher temperatures did small Bragg peaks at 33.15° and 35.61° 2θ start to develop concomitantly with a decrease in the background intensity. These new peaks correspond to the most intense Bragg peaks of α-Fe_2O_3 (hematite; ICDD PDF 33-0664, $a = 5.03$ Å, $c = 13.74$ Å). Once the crystallization of α-Fe_2O_3 was initiated, the only observed changes with temperature were a reduction in width and an increase in intensity of the α-Fe_2O_3 peaks up to ~500 °C. From 500 to 1,000 °C, the intensity of the

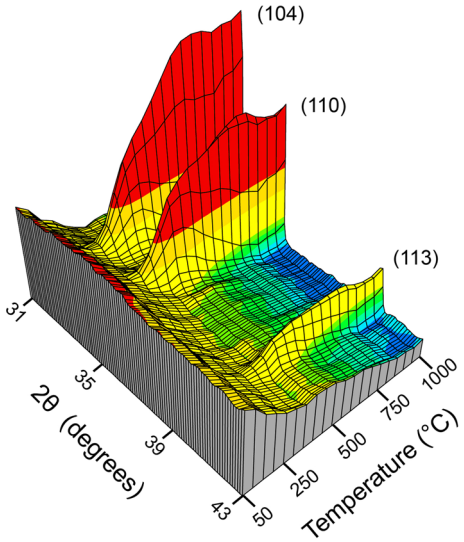

Fig. 4 3D X-ray diffraction plot showing the transformation of carbonated 2-line ferrihydrite to α-Fe_2O_3 with increasing annealing temperature

Bragg peaks remained constant, but they became narrower as the temperature increased. No other crystalline solids were observed during the reaction. The refinement of the X-ray diffraction patterns of samples obtained at 350, 600, 800, and 1,000 °C (Fig. 5) confirmed that they are all consistent with only α-Fe_2O_3. An evaluation of the Scherrer crystallite size showed a linear increase of the crystallite size with temperature from 20 nm at 350 °C to 131 nm at 1,000 °C (Table 2; Fig. SI-2). High-resolution microscopy revealed the morphologies of the α-Fe_2O_3 samples, as well as the particle sizes and internal structures (Figs. 6, 7). At 350 °C (Figs. 6a, 7a) and 600 °C (Figs. 6b, 7c), the particles have a pseudospheric morphology, but at 800 °C (Fig. 6c) and 1,000 °C (Fig. 6d) they are prismatic. The average particle dimensions were evaluated by measuring the width (W) and length (L) of 100 particles in each sample (Fig. SI-3). The particle sizes increased from 20 ± 6 (L) × 15 ± 4 (W) nm at 350 °C to 352 ± 119 (L) × 277 ± 103 (W) nm at 1,000 °C (Table 2). HR-TEM images of α-Fe_2O_3 confirmed that the particles were crystalline with interplanar spacings of ~3.7, 2.7, 2.2, and 1.7 Å visible (Fig. 7), which correspond to the (012), (104), (113), and (116) d-spacings of α-Fe_2O_3. The SAED patterns (insets in Fig. 7) corroborate the temperature-dependent increase in Scherrer crystallite size (Figs. 4, 5; Table 2). The SAED pattern of the sample produced at 350 °C (Fig. 7b, inset) showed diffuse diffraction rings with poorly developed spots, evidencing the presence of very small, nanocrystalline particles. In contrast, only discrete spots were observed in samples produced at higher temperatures (e.g., Fig. 7h, inset). The HR-TEM images also revealed temperature-dependent structural differences at the nanoscale: at 350 °C the average particle size was of 20 × 15 nm (Fig. 7a, b), matching the Scherrer crystallite sizes. At 600 °C, the average particle size was ~71 × 52 nm (Fig. 7c, d), which is slightly larger than the Scherrer crystallite size (~55 nm). However, the sizes of the prismatic particles obtained at 800 and 1,000 °C (Figs. 6c, d, 7e, g) were much larger (202 × 136 and 352 × 277 nm, respectively) than their Scherrer crystallite sizes (92 and 131 nm, respectively). This revealed that a significant number of the prismatic particles were made of nanocrystalline subparticles of various sizes down to ~20 nm (e.g., Fig. 7i, j). These data indicate that α-Fe_2O_3 synthesized from carbonated 2-line ferrihydrite at lower temperatures (350–600 °C) grows as single nanocrystals. In contrast, at higher temperatures (800–1,000 °C) the formed α-Fe_2O_3 particles consist of aggregates of nanocrystalline subparticles (Rath et al. 1999).

Table 2 Microstructural-dependent magnetic properties of α-Fe_2O_3 nanoparticles obtained from carbonated 2-line ferrihydrite. Hc is the magnetic coercive field, while Mr is the remanent magnetization

Temp. (°C)	Heating time (h)	Morphology	Size (nm)[a] L (length), W (width)	Scherrer crystallite size (nm)	Hc (Oe)[b]	Mr (emu/g)
350	8	Pseudospheric	$L = 20 \pm 6$, $W = 15 \pm 4$	20 (1)	289 ± 29	0.007 (1)
600	13	Pseudospheric	$L = 71 \pm 19$, $W = 52 \pm 16$	55 (3)	1,720 ± 207	0.033 (5)
800	16	Prismatic	$L = 202 \pm 101$, $W = 136 \pm 46$	92 (4)	3,837 ± 123	0.011 (4)
1,000	20	Prismatic	$L = 352 \pm 109$, $W = 277 \pm 103$	131 (6)	5,027 ± 46	0.025 (5)

[a] Values correspond to the average and standard deviation of 100 nanoparticles

[b] Values correspond to the average and standard deviation of 4 magnetic coercivity measurements

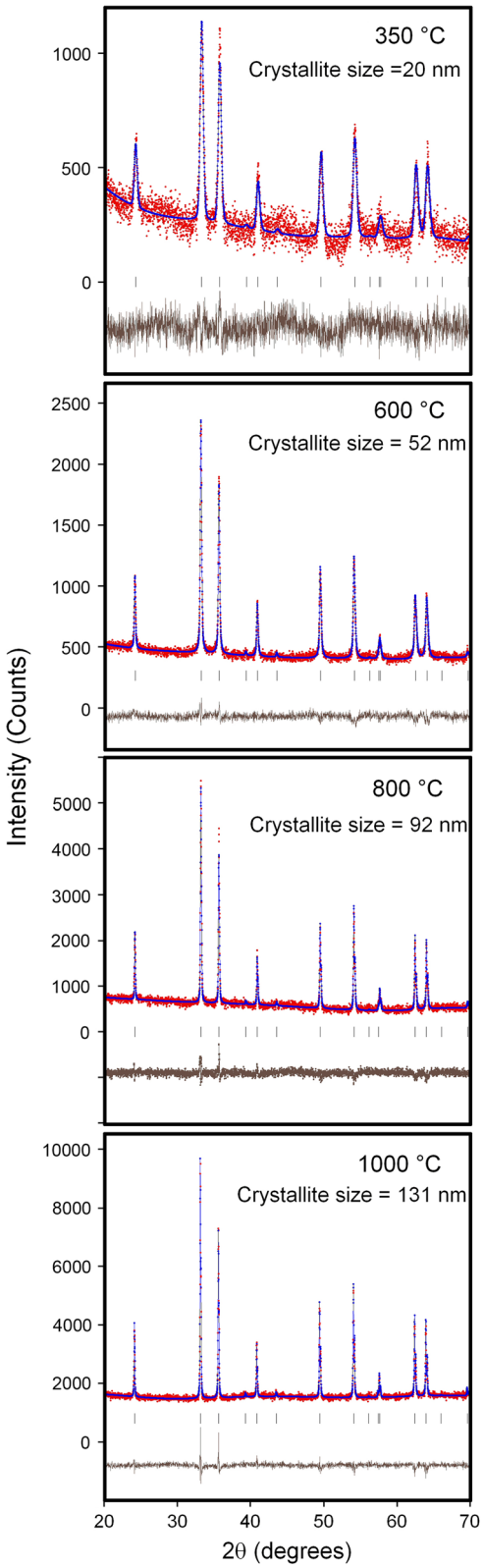

◀**Fig. 5** Pattern-matching refinements of the powder X-ray diffraction patterns of α-Fe_2O_3 after the dry heat treatment at 350, 600, 800, and 1,000 °C. Points correspond to the experimental data; the *solid lines* are the calculated profiles. *Tick marks* below the patterns represent the positions of allowed reflections. The difference *curves* are plotted at the *bottom* of the patterns showing the difference between the experimental and calculated profiles

The magnetic measurements of crystalline end product α-Fe_2O_3 also revealed a synthesis-temperature-dependent behavior (Fig. 8, Table 2). The α-Fe_2O_3 sample obtained at 350 °C exhibited a very small hysteresis loop with a remanent magnetization (Mr) of 0.007(1) emu/g and coercivity (Hc) of only ∼289 Oe. Conversely, the hysteresis loop of the sample crystallized at 600 °C showed a weak ferromagnetic behavior with a remanent magnetization of 0.032(5) emu/g, but a higher magnetic coercivity of ∼1,720 Oe while at 800 and 1,000 °C very wide-open hysteresis loops, indicating a stronger ferromagnetic behavior with remanent magnetization and coercivity values of 0.011(4) emu/g and ∼3,837 Oe (800 °C) and 0.025(5) emu/g and ∼5,027 Oe (1,000 °C), respectively, were observed. Note, however, that the hysteresis loops did not reach magnetization saturation, even at the maximum applied magnetic field. Nonetheless these data clearly indicate a drastic change in magnetic properties with increasing crystallization temperature.

The understanding of this temperature-dependent magnetic behavior requires comparison with the nanoscale structural characteristics of the α-Fe_2O_3. Figure 9 shows the variation of magnetic coercivity with particle size, Scherrer crystallite size, and temperature. There is a linear proportionality between coercivity and Scherrer crystallite size and between coercivity, magnetization energy density and temperature, but the relationship between the coercivity and particle size follows a logarithmic trend. Although our results regarding these trends are in agreement with several studies (Rath et al. 1999; Bercoff and Bertorello 2010; Sahu et al. 1997; Bao et al. 2011), the dependence between magnetic coercivity, temperature, and particle size is still a matter of debate. Using different synthesis methods various other authors have reported decreasing coercivity values with increasing particle sizes (Jacob and Khadar 2010; Kletetschka and Wasilewski 2002; Li et al. 2002; Yao and Cao 2012). This has also been observed in natural α-Fe_2O_3,

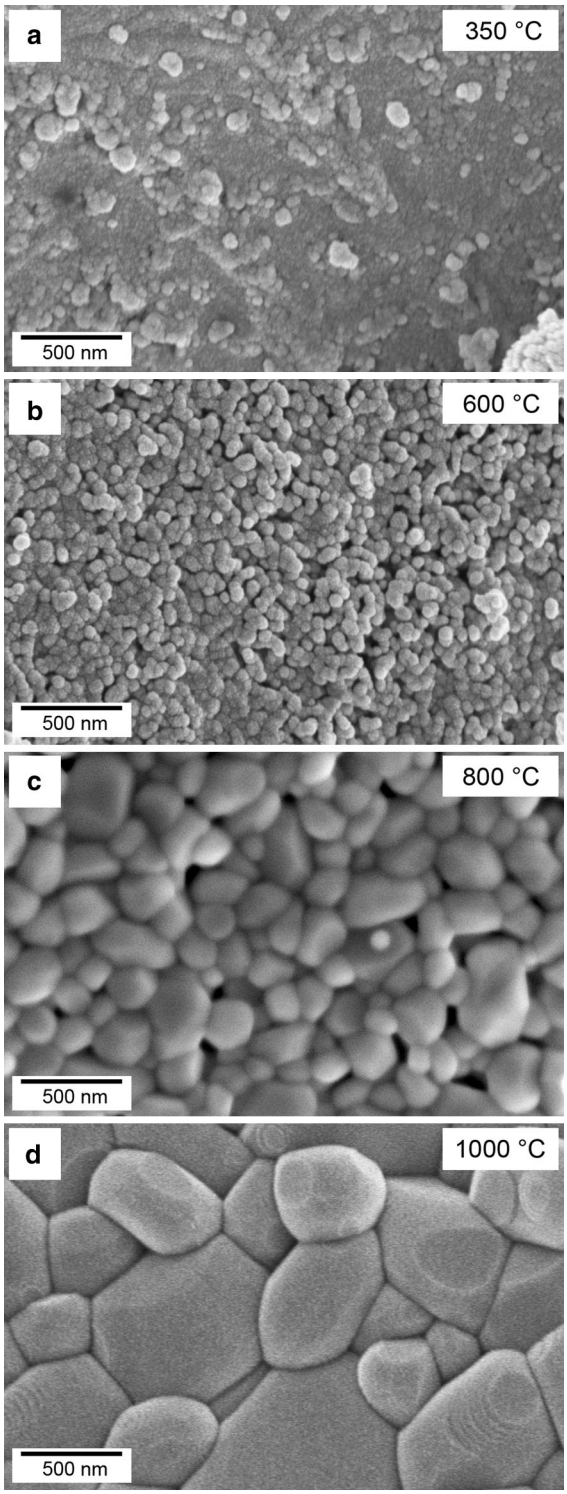

Fig. 6 Secondary electron FEG-SEM images of the α-Fe_2O_3 samples produced at 350 (**a**), 600 (**b**), 800 (**c**), and 1,000 °C (**d**)

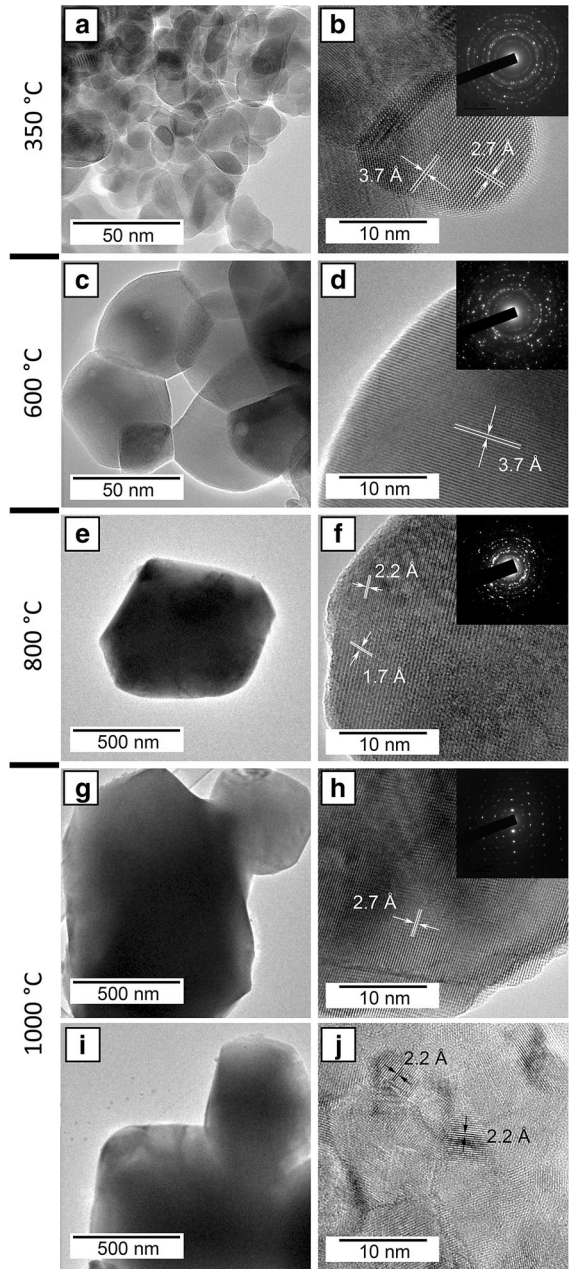

Fig. 7 HR-TEM microphotographs and corresponding SAED patterns of α-Fe_2O_3 samples produced at 350 (**a**, **b**), 600 (**c**, **d**), 800 (**e**, **f**), and 1,000 °C (**g**, **h**). α-Fe_2O_3 nanoparticles with a subparticle structure with sizes down to $\sim$20 nm (**i**, **j**)

with a very gradual decrease in coercivity at sizes above 100 μm (Kletetschka and Wasilewski 2002). Interestingly, the effect of thermally induced growth on the coercivity field and magnetization energy

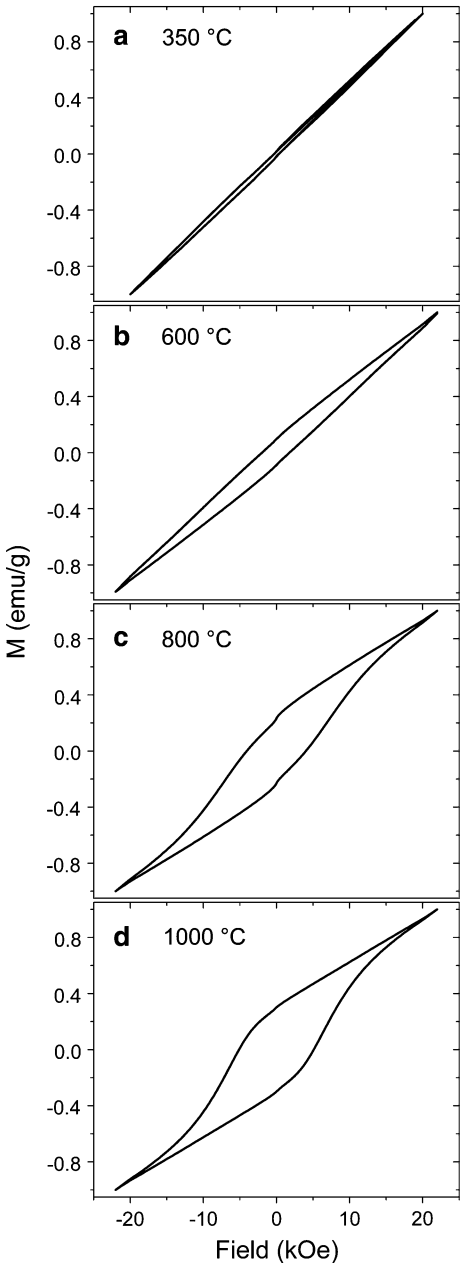

Fig. 8 Hysteresis loops of the α-Fe_2O_3 nanoparticles obtained at 350 (**a**), 600 (**b**), 800 (**c**), and 1,000 °C (**d**)

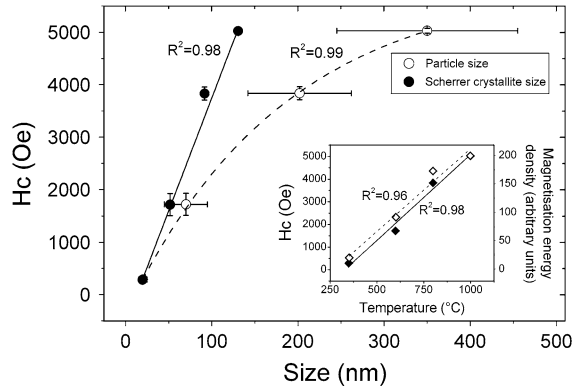

Fig. 9 Variation of coercivity with particle size and Scherrer crystallite size. *Horizontal error bars* in particle size data correspond to the standard deviation of 100 measurements. *Vertical error bars* correspond to the standard deviation of four coercivity measurements. *Inset* shows the variation of the coercivity and magnetization energy density with temperature

density has been addressed for Ni thin films. Kumar et al. (2009) and Kumar (2010) reported that the magnetic behavior of Ni thin films was dependent on grain size, in particular on the width of the grain boundary walls. By using atomic force microscopy, they revealed that the thermally induced increase of the grain size produced a densification of the solid which was translated into a decrease of the width of the grain boundaries. This transition from a nanocrystalline to crystalline structure caused a maximum in the coercive field, which then decreased with increase of particle size, similarly to other Fe- or Co-bearing alloys and compounds (Cullity and Graham 2008). Our high-resolution microscopy images of α-Fe_2O_3 (Figs. 6, 7) revealed a progressive decrease of the width of the grain boundary sizes with temperature. Also the dependence of the magnetic coercivity on the particle size of α-Fe_2O_3 followed a logarithmic trend (Fig. 9), so we hypothesize that the maximum of the coercivity field in our system was not reached. This maximum and a subsequent decrease of the magnetic coercivity may occur at temperatures above 1,000 °C and after longer annealing times.

However, compared to our dry-heating experiments, many researches for α-Fe_2O_3 have been carried out on synthetic hematite obtained under hydrothermal conditions. For example, hematite nanodiscs (ϕ = 78–150 nm) obtained hydrothermally from $FeCl_3$, NaH_2PO_4, and ethanol glycol at 200 °C reached coercivity values between 22 and 214 Oe. Hydrothermal synthesis (70–180 °C) of α-Fe_2O_3 using ferrihydrite as a precursor resulted in coercivity values between 670 and 2,600 Oe after reaction times between 2 h and 44 days (Liu et al. 2010). Some researchers explain these magnetic properties as a consequence of magnetocrystalline and/or magnetoelastic anisotropies. However, in the literature there is

plethora of research about the synthesis of α-Fe_2O_3 with many different morphologies whose coercivity values are explained by shape anisotropy (e.g., An et al. 2012; Pan et al. 2009; Muruganandham et al. 2011; Liu et al. 2011; Rath et al. 1999; Tsuzuki et al. 2011; Tadic et al. 2012; Xu et al. 2009; Bercoff and Bertorello 2010; Suber et al. 2010; Chang et al. 2010; Xu et al. 2013; Zhang et al. 2013). Anisotropic particle morphologies induce high magnetic coercivities because the magnetic spins are preferentially aligned along the easy magnetic axes and their reversals to other directions require more energy in comparison with spherical or pseudospherical particles (An et al. 2012; Pan et al. 2009; Tadic et al. 2012; Mitra et al. 2007; Zeng et al. 2007). In our experiments, the morphology of the α-Fe_2O_3 changed from pseudospherical to prismatic with increasing temperature. However, the length/width ratio of our particles was very similar (~1.3) throughout, showing no significant variations across the whole temperature range between 350 and 1,000 °C. We cannot discard a contribution of shape anisotropy to the coercivity of our α-Fe_2O_3; however, we consider that in our experiments the effect of temperature on the shape anisotropy is very small or negligible.

Nevertheless, in our experiments, temperature played an important role on controlling the particle and Scherrer crystallite size growth (Fig. SI-2). Considering that the crystallization of α-Fe_2O_3 started at ~250 °C (Fig. 4) and the rate of heating for all the samples were the same (1 °C/min), our data (Table 2; Fig. SI-2) indicate that the growth of the Scherrer crystallite sizes with temperature took place at a slower rate (~0.17 nm/ °C) than the growth of the particle sizes (~0.43 nm/ °C). These different growth rates are translated into a progressive, temperature-dependent, development of a subparticle structure, i.e., from single nanocrystals at 350 °C to aggregates of nanocrystalline subparticles at 1,000 °C (Fig. 7). Our HR-TEM images also suggest that the subparticles observed at 800–1,000 °C (Fig. 7i, j) were relicts of the single nanocrystals observed at 350 °C (Fig. 7a, b), and this is a result of the intergrowth and aggregation of these single nanocrystals during the dry-heating process. It is thus also not surprising that the growth of these aggregates with a subparticle structure permits stronger magnetic interactions: the unusual high coercivity reached at 800–1,000 °C is most likely a consequence of the contribution of the individual subparticles as well as the contribution from the interactions between these particles (Rath et al. 1999; Tadic et al. 2012). At lower temperature, this subparticle structure is completely absent and therefore the low coercivity values are only a consequence of the contribution of the single nanocrystals.

Conclusions

This study demonstrates that enhanced magnetic coercivities for α-Fe_2O_3 can be achieved using a facile method, consisting of dry-heating a carbonated 2-line ferrihydrite precursor prepared from solution. α-Fe_2O_3 exhibited temperature-dependent magnetic coercivity values ranging from 289 to 5,027 Oe. The origin of these high coercivity values is interpreted as being a consequence of the slower growth rate of the Scherrer crystallite size with respect to the particle size during the heating process. These differences in the growth rates are also translated into a progressive development of a subparticle structure at the nanoscale. At lower temperatures (350–600 °C), single particles crystallize however; at higher temperatures (>600 °C), the growth of crystalline aggregates with a subparticle structure is favoured.

Acknowledgments This research was supported by the Spanish Ministry of Economy and Competitivity (MICINN-12-MAT2011-27573-C04-02) and the Marie Curie EU-FP6 MINGRO Research and Training Network under contract MRTNCT-2006-035488. The authors would like to thank the Cohen Laboratories at the School of Earth and Environment and the Leeds Electron Microscopy and Spectroscopy Centre (LEMAS) at the Faculty of Engineering (University of Leeds). The help of David Martínez Blanco (Scientific-Technical Services of the University of Oviedo, Spain) with the magnetic measurements is also acknowledged.

References

An Z, Zhang J, Pan S, Song G (2012) Novel peanut-like α-Fe2O3 superstructures: oriented aggregation and Ostwald ripening in a one-pot solvothermal process. Powder Technol 217:274–280. doi:10.1016/j.powtec.2011.10.038

Andersen FA, Brečević L (1991) Infrared spectra of amorphous and crystalline calcium carbonate. Acta Chem Scand 45:1018–1024. doi:10.1002/chin.199209005

Bahgat M, Khedr MH, Nasr MI, Sedeek EK (2006) Effect of temperature on reduction of nanocrystalline Fe_2O_3 into metallic iron. Mater Sci Tech Ser 22:315–320. doi:10.1179/026708306X81559

Bao L, Yang H, Wang X, Zhang F, Shi R, Liu B, Wang L, Zhao H (2011) Effect of temperature on reduction of nanocrystalline Fe_2O_3 into metallic iron. J Cryst Growth 328:62–69. doi:10.1016/j.jcrysgro.2011.05.030

Bercoff PG, Bertorello HR (2010) Magnetic properties of hematite with large coercivity. App Phys A 100:1019–1027. doi:10.1007/s00339-010-5983-7

Berquó TS, Banerjee SK, Ford RG, Penn RL, Pichler T (2007) High crystallinity Si-ferrihydrite: an insight into its neel temperature and size dependence of magnetic properties. J Geophys Res 112:B02102. doi:10.1029/2006JB004583

Carta D, Casula MF, Corrias A, Falqui A, Navarra G, Pinna G (2009) Structural and magnetic characterization of synthetic ferrihydrite nanoparticles. Mater Chem Phys 113: 349–355. doi:10.1016/j.matchemphys.2008.07.122

Chang C, Zhang C, Wang W, Li Q (2010) Preparation and magnetic properties of Fe_2O_3 microtubules prepared by sol-gel template method. Rare Met 29:501–504. doi:10.1007/s12598-010-0156-6

Coelho AA (2003) TOPAS: General profile and structure analysis software for powder diffraction data

Cornell RM, Schwertmann U (2003) The iron oxides: structure, properties, reactions and occurrences and uses. Wiley-VCH, Weinheim

Cullity BD, Graham CD (2008) Introduction to magnetic materials. Wiley-IEEE Press, Piscataway

Davidson LE, Shaw S, Benning LG (2008) The kinetics and mechanisms of schwertmannite transformation to goethite and hematite under alkaline conditions. Am Mineral 93: 1326–1337. doi:10.2138/am.2008.276

Eggleton RA, Fitzpatrick RW (1988) New data and a revised structural model for ferrihydrite. Clay Clay Miner 36:111–124. doi:10.1346/CCMN.1988.0360203

Fang XL, Chen C, Jin MS, Kuang Q, Xie ZX, Xie SY, Huang RB, Zheng LS (2009) Single-crystal-like hematite colloidal nanocrystal clusters: synthesis and applications in gas sensors, photocatalysis and water treatment. J Mater Chem 19:6154–6160. doi:10.1039/b905034e

Farmer VC (1974) The infrared spectra of minerals. Mineralogical society monograph, vol 4. Mineralogical Society of Great Britain & Ireland, Twickenham

Galwey AK, Brown ME (1999) Decomposition of carbonates. Thermal decomposition of ionic solids. Elsevier B.V. Ed, In, pp 345–364

Gubin SP, Koksharov YA, Khomutov GB, Yurkov GY (2005) Magnetic nanoparticles: preparation, structure and properties. Russ Chem Rev 74:489–520. doi:10.1070/RC2005v074n06ABEH000897

Guo P, Wei Z, Wang B, Ding Y, Li H, Zhang G, Zhao XS (2011) Controlled synthesis, magnetic and sensing properties of hematite nanorods and microcapsules. Colloid Surf A 380: 234–240. doi:10.1016/j.colsurfa.2011.02.026

Islam MS, Kusumoto Y, Abdulla-Al-Mamun M (2012) Novel rose-type magnetic (Fe_3O_4, γ-Fe_2O_3 and α-Fe_2O_3) nanoplates synthesized by simple hydrothermal decomposition. Mater Lett 66:165–167. doi:10.1016/j.matlet.2011.08.057

Jacob J, Khadar MA (2010) VSM and Mössbauer study of nanostructured hematite. J Magn Magn Mater 322: 614–621. doi:10.1016/j.jmmm.2009.10.025

Jia XH, Song HJ (2012) Facile synthesis of monodispersed α-Fe_2O_3 microspheres through template-free hydrothermal route. J Nanopart Res 14:663. doi:10.1007/s11051-011-0663-x

Jia X, Yang L, Song H, Su Y (2011) Facile synthesis and magnetic properties of cross α-Fe_2O_3 nanorods. Micro Nano Lett 6:806–808. doi:10.1049/mnl 2011.0367

Kletetschka G, Wasilewski PJ (2002) Grain size limit for SD hematite. Phys Earth Planet In 129:173–179. doi:10.1016/S0031-9201(01)00271-0

Kumar P (2010) Magnetic behavior of surface nanostructured 50-nm nickel thin films. Nanoscale Res Lett 5:1596–1602. doi:10.1007/s11671-010-9682-2

Kumar P, Krishna MG, Bhattacharya AK (2009) Effect of microstructural evolution on magnetic properties of Ni thin films. Bull Mater Sci 32:263–270. doi:10.1007/s12034-009-0040-x

Li GS, Smith RL Jr, Inomata H, Arai K (2002) Preparation and magnetization of hematite nanocrystals with amorphous iron oxide layers by hydrothermal conditions. Mater Res Bull 37:949–955. doi:10.1016/S0025-5408(02)00695-5

Li L, Chu Y, Liu Y (2007) Synthesis and characterization of ring-like α-Fe_2O_3. Nanotechnology 18:105603. doi:10.1088/0957-4484/18/10/105603

Li Z, Lai X, Wang H, Mao D, Xing C, Wang D (2009) Direct hydrothermal synthesis of single-crystalline hematite nanorods assisted by 1,2-propanediamine. Nanotechnology 20:245603. doi:10.1088/0957-4484/20/24/245603

Liu Q, Barrón V, Torrent J, Eeckhout SG, Deng C (2008) Magnetism of intermediate hydromaghemite in the transformation of 2-line ferrihydrite into hematite and its paleoenvironmental implications. J Geophys Res 113: B01103. doi:10.1029/2007JB005207

Liu H, Li P, Lu B, Wei Y, Sun Y (2009) Transformation of ferrihydrite in the presence or absence of trace Fe(II): the effect of preparation procedures of ferrihydrite. J Solid State Chem 182:1767–1771. doi:10.1016/j.jssc.2009.03.030

Liu Q, Barrón V, Torrent J, Qin H, Yu Y (2010) The magnetismo of micro-sized hematite explained. Phys Earth Planet In 183:387–397. doi:10.1016/j.pepi.2010.08.008

Liu C, Ma J, Liu Y (2011) Formation mechanism and magnetic properties of three different hematite nanostructures synthesized by one-step hydrothermal procedure. Sci China Chem 54:1607–1614. doi:10.1007/s11426-011-4392-x

Lovesey SW, Rodríguez-Fernández A, Blanco JA (2011) Parity-odd multipoles, magnetic charges, and chirality in hematite α-Fe_2O_3. Phys Rev B 83:054427. doi:10.1103/PhysRevB.83.054427

Lu BL, Xu XY, Wu D, Sun YH (2008) Preparation and characterization of porous alpha-Fe_2O_3 nanodisks. Chin J Inorg Chem 24:1690–1694

Michel FM, Barrón V, Torrent J, Morales MP, Serna CJ, Boily JF, Liu Q, Ambrosini A, Cismasu AC, Brown GE Jr (2010) Ordered ferrimagnetic form of ferrihydrite reveals links among structure, composition, and magnetism. P Natl Acad Sci USA 107:2787–2792. doi:10.1073/pnas.0910170107

Mitra S, Das S, Mandal K, Chaudhuri S (2007) Synthesis of a α-Fe_2O_3 nanocrystals in its different morphological attributes: grow mechanism, optical and magnetic properties. Nanotechnology 18:275608. doi:10.1088/0957-4484/18/27/275608

Muruganandham M, Amutha R, Sathish M, Singh TS, Suri RPS, Sillanpää MJ (2011) Facile fabrication of hierarchical α-Fe_2O_3: self-assembly and its magnetic and electrochemical properties. Phys Chem C 115:18164–18173. doi:10.1021/jp205834m

Ni S, Lin S, Pan Q, Yang F, Huang K, Wang X, He D (2009) Synthesis of core–shell α-Fe_2O_3 hollow micro-spheres by a simple two-step process. J Alloy Compd 478:876–879. doi:10.1016/j.jallcom.2008.12.038

Ni H, Ni Y, Zhou Y, Hong J (2012) Microwave–hydrothermal synthesis, characterization and properties of rice-like α-Fe_2O_3 nanorods. Mater Lett 73:206–208. doi:10.1016/j.matlet.2012.01.065

Pan Q, Huang K, Ni S, Yang F, Lin S, He D (2009) Synthesis of α-Fe_2O_3 dendrites by a hydrothermal approach and their application in lithium-ion batteries. J Phys D Appl Phys 42:015417. doi:10.1088/0022-3727/42/1/015417

Peng D, Beysen S, Li Q, Sun Y, Yang L (2010) Hydrothermal synthesis of monodisperse α-Fe_2O_3 hexagonal platelets. Particuology 8:386–389. doi:10.1016/j.partic.2010.05.003

Raiswell R, Vu HP, Brinza L, Benning LG (2010) The determination of Fe in ferrihydrite by ascorbic acid extraction: methodology, dissolution kinetics and loss of solubility with age and de-watering. Chem Geol 278:70–79. doi:10.1016/j.chemgeo.2010.09.002

Rath C, Sahu KK, Kulkarni SD, Anand S, Date SK, Das RP, Mishra NC (1999) Microstructure-dependent coercivity in monodispersed hematite particles. Appl Phys Lett 75:4171–4173. doi:10.1063/1.125572

Rodriguez-Blanco JD, Shaw S, Benning LG (2008) How to make 'stable' ACC: protocol and preliminary structural characterization. Mineral Mag 72:283–286. doi:10.1180/minmag.2008.072.1.283

Roncal-Herrero T, Rodriguez-Blanco JD, Benning LG, Oelkers EH (2009) Precipitation or iron and aluminum phosphates directly from aqueous solution as a function of temperature from 50 to 200 & #xB0;C. Cryst Growth Des 9:5197–5205. doi:10.1021/cg900654m

Rout K, Mohapatra M, Anand S (2012) 2-Line ferrihydrite: synthesis, characterization and its adsorption behavior for removal of Pb(II), Cd(II), Cu(II) and Zn(II) from aqueous solutions. Dalton Trans 41:3302–3312. doi:10.1039/c2dt11651k

Sahu KK, Rath C, Mishra NC, Anand S, Das RP (1997) Microstructural and magnetic studies on hydrothermally prepared hematite. J Colloid Interface Sci 185:402–410. doi:10.1006/jcis 1996.4525

Scherrer P (1918) Estimation of the size and internal structure of colloidal particles by means of röntgen. Nachr Ges Wiss Götingen Math-Pys Kl 2:96–100

Schneeweiss O, Grygar T, David B, Zboril R, Filip J, Mashlan M (2008) Mössbauer and magnetic studies of nanocrystalline iron, iron oxide and iron carbide powders prepared from synthetic ferrihydrite. AIP Conf Proc 1070:106–113. doi:10.1063/1.3030834

Schwertmann U, Taylor RM (1972) The transformation of lepidocrocite to goethite. Clay Clay Miner 20:151–158. doi:10.1346/CCMN.1972.0200306

Song F, Guan J, Fan X, Yan G (2009) Single-crystal star-like arrayed particles of hematite: synthesis, formation mechanism and magnetic properties. J Alloy Compd 485:753–758. doi:10.1016/j.jallcom.2009.06.075

Song HJ, Li N, Shen XQ (2011) Template-free synthesis of hollow α-Fe_2O_3 microspheres. Appl Phys A-Mater 102:559–563. doi:10.1007/s00339-010-6072-7

Stanjek H, Weidler PG (1992) The effect of dry heating on the chemistry, surface area, and oxalate solubility of synthetic 2-line and 6-line ferrihydrites. Clay Miner 27:397–412. doi:10.1180/claymin.1992.027.4.01

Suber L, Imperatori P, Mari A, Marchegiani G, Mansilla MV, Fiorani D, Plunkett WR, Rinaldi D, Cannas C, Ennas G, Peddis D (2010) Thermal hysteresis of Morin transition in hematite particles. Phys Chem Chem Phys 12:6984–6989. doi:10.1039/b925371h

Suresh R, Vijayaraj A, Giribabu K, Manigandan R, Prabu R, Stephen A, Thirumal E, Narayanan V (2013) Fabrication of iron oxide nanoparticles: magnetic and electrochemical sensing property. J Mater Sci-Mater El 24:1256–1263. doi:10.1007/s10854-012-0916-1

Tadic M, Citakovic N, Panjan M, Stanojevic B, Markovic D, Jovanovic D, Spasojevic V (2012) Syntesis, morphology, microstructure and magnetic properties of hematite submicron particles. J Alloy Compd 543:118–124. doi:10.1016/j.jallcom.2012.07.047

Tadić M, Čitaković N, Panjan M, Stojanović Z, Marković D, Spasojević V (2011) Synthesis, morphology, microstructure and magnetic properties of hematite submicron particles. J Alloy Compd 509:7639–7644. doi:10.1016/j.jallcom.2011.04.117

Tsuzuki T, Schäffel F, Muroi M, McCormick PG (2011) α-Fe_2O_3 nano-platelets prepared by mechanochemical/termal processing. Powder Technol 210:198–202. doi:10.1016/j.powtec.2011.03.012

Vallina B, Rodriguez-Blanco JD, Brown AP, Blanco JA, Benning LG (2013) Amorphous dysprosium carbonate: characterization, stability, and crystallization pathways. J Nanopart Res 15:1438. doi:10.1007/s11051-013-1438-3

Vu HP, Shaw S, Brinza L, Benning LG (2010) Crystallization of hematite (α-Fe_2O_3) under alkaline condition: the effects of Pb. Cryst Growth Des 10:1544–1551. doi:10.1021/cg900782g

Wang H, Geng WC, Wang Y (2011) Preparation of nanoparticles and hollow spheres of alpha-Fe_2O_3 and their properties. Res Chem Intermediat 37:389–395. doi:10.1007/s11164-011-0269-z

Xu JS, Zhu YJ (2012) α-Fe_2O_3 hierarchically nanostructured mesoporous microspheres: surfactant-free solvothermal combined with heat treatment synthesis, photocatalytic activity and magnetic property. CrystEngComm 14:2702–2710. doi:10.1039/C2CE06473A

Xu YY, Zhao D, Zhang XJ, Jin WT, Kashkarov P, Zhang H (2009) Synthesis and characterization of single-crystalline α-Fe_2O_3 nanoleaves. Physica E 41:806–811. doi:10.1016/j.physe.2008.12.015

Xu W, Hausner DB, Harrington R, Lee PL, Strongin DR, Parise JB (2011) Structural water in ferrihydrite and constraints this provides on possible structure models. Am Mineral 96:513–520. doi:10.2138/am 2011.3460

Xu JS, Zhu YL, Chen F (2013) Solvothermal synthesis, characterization and magnetic properties of α-Fe_2O_3 and Fe_3O_4 flower-like hollow microspheres. J Solid State Chem 199:204–211. doi:10.1016/j.jssc.2012.12.027

Yadav LDS (2005) Organic spectroscopy. Anamaya Publishers, New Delhi

Yang Y, Yi JB, Huang XL, Xue JM, Ding J (2011) High-coercivity in α-Fe_2O_3 formed after annealing from Fe_3O_4 formed nanoparticles. IEEE T Magn 47:3340–3342. doi:10.1109/TMAG.2011.2159487

Yao R, Cao C (2012) Self-assembly of α-Fe_2O_3 mesocrystals with high coercivity. RSC Adv 2:1979–1985. doi:10.1039/c2ra00796g

Yu JY, Park M, Kim J (2002) Solubilities of synthetic schwertmannite and ferrihydrite. Geochem J 36:119–132

Zeng S, Tang K, Li T (2007) Controlled synthesis of α-Fe_2O_3 nanorods and its size-dependent optical absorption, electrochemical, and magnetic properties. J Colloid Interface Sci 312:513–521. doi:10.1016/j.jcis.2007.03.046

Zhang ZJ, Chen XY (2009) Magnetic greigite (Fe_3S_4) nanomaterials: shape-controlled solvothermal synthesis and their calcination conversion into hematite (α-Fe_2O_3) nanomaterials. J Alloy Compd 488:339–345. doi:10.1016/j.jallcom.2009.08.127

Zhang YC, Tang JY, Hu XY (2008) Controllable synthesis and magnetic properties of pure hematite and maghemite nanocrystals from a molecular precursor. J Alloy Compd 462:24–28. doi:10.1016/j.jallcom.2007.07.115

Zhang XH, Chen YZ, Liu H, Wei Y, Wei W (2013) Controllable synthesis, formation mechanism and magnetic properties of hierarchical alpha-Fe_2O_3 with various morphologies. J Alloy Compd 55:74–81. doi:10.1016/j.jallcom.2012.12.025

Zhao J, Huggins FE, Feng Z, Huffman GP (1994) Ferrihydrite: surface structure and its effects on phase transformation. Clay Clay Miner 42:737–746

Zhong SL, Song JM, Zhang S, Yao H, Xu AW, Yao WT, Yu SH (2008) Template-free hydrothermal synthesis and formation mechanism of hematite microrings. J Phys Chem C 112:19916–19921. doi:10.1021/jp806665b

Zhu LP, Xiao HM, Liu XM, Fu SY (2006) Template-free synthesis and characterization of novel 3D urchin-like α-Fe2O3 superstructures. J Mater Chem 16:1794–1797. doi:10.1039/b604378j

Zhu W, Cui X, Wang L, Liu T, Zhang Q (2011) Monodisperse porous pod-like hematite: hydrothermal formation, optical absorbance, and magnetic properties. Mater Lett 65:1003–1006. doi:10.1016/j.matlet.2010.12.053